

ASME Journal of Manufacturing Science and Engineering Online journal at:

https://asmedigitalcollection.asme.org/manufacturingscience



Zhi Zhang

Department of Mechanical and Aerospace Engineering, Ohio State University, Columbus, OH 43210 e-mail: zhang.3137@osu.edu

Antony George

Department of Mechanical and Aerospace Engineering, Ohio State University, Columbus, OH 43210 e-mail: george.888@osu.edu

Md. Ferdous Alam

Department of Mechanical and Aerospace Engineering, Ohio State University, Columbus, OH 43210 e-mail: alam.92@osu.edu

Chris Eubel

Department of Mechanical and Aerospace Engineering, Ohio State University, Columbus, OH 43210 e-mail: eubel.1@osu.edu

Chaitanya Krishna Prasad Vallabh

Department of Mechanical Engineering, Stevens Institute of Technology, Hoboken, NJ 07030 e-mail: cvallabh@stevens.edu

Max Shtein

Department of Materials Science,
University of Michigan,
Ann Arbor, MI 48109
e-mail: mshtein@umich.edu

Kira Barton

Department of Mechanical Engineering, University of Michigan, Ann Arbor, MI 48109 e-mail: bartonkl@umich.edu

David J. Hoelzle'

Department of Mechanical and Aerospace Engineering, Ohio State University, Columbus, OH 43210 e-mail: hoelzle.1@osu.edu

An Additive Manufacturing Testbed to Evaluate Machine Learning-Based Autonomous Manufacturing

This paper details the design and operation of a testbed to evaluate the concept of autonomous manufacturing to achieve a desired manufactured part performance specification. This testbed, the autonomous manufacturing system for phononic crystals (AMSPnC), is composed of additive manufacturing, material transport, ultrasonic testing, and cognition subsystems. Critically, the AMSPnC exhibits common manufacturing deficiencies such as process operating window limits, process uncertainty, and probabilistic failure. A case study illustrates the AMSPnC function using a standard supervised learning model trained by printing and testing an array of 48 unique designs that span the allowable design space. Using this model, three separate performance specifications are defined and an optimization algorithm is applied to autonomously select three corresponding design sets to achieve the specified performance. Validation manufacturing and testing confirms that two of the three optimal designs, as defined by an objective function, achieve the desired performance, with the third being outside the design window in which a distinct bandpass is achieved in phononic crystals (PnCs). Furthermore, across all samples, there is a marked difference between the observed bandpass characteristics and predictions from finite elements method computation, highlighting the importance of autonomous manufacturing for complex manufacturing objectives. [DOI: 10.1115/1.4064321]

Keywords: additive manufacturing, computer-integrated manufacturing, control and automation, inspection and quality control

Manuscript received May 17, 2023; final manuscript received December 11, 2023; published online January 12, 2024. Assoc. Editor: Jaydeep Karandikar.

¹Corresponding author.

1 Introduction

This paper details the design and methods for a testbed to evaluate the concept of autonomous manufacturing. Here, we describe autonomous manufacturing as an intelligent manufacturing system that can make its own decisions to manufacture a part with some desired performance metric without any human intervention. To communicate what we define as autonomous manufacturing, we first provide a simple example. Consider the simple production objective of the manufacture of a bracket with a specified load and moment capacity in all three directions. The traditional manufacturing paradigm would require: materials selection, first principles engineering analysis with assumed material properties, three-dimensional (3D) computational analysis, production design and analysis, production, testing-based validation, and then design and process iteration, as necessary. Process iteration often applies the design of experiments (DoEs) approach [1], which is well understood and effective, but has significant material and labor costs. Now consider an alternative, autonomous manufacturing paradigm (Fig. 1): parameterize the part design and material variables, use a flexible manufacturing system with integrated metrology and machine learning (ML)-based cognition to iteratively manufacture within the design space, and then test performance to converge to a part that satisfies the production objective, while validating the part.

The simple and well-understood production objective for the bracket manufacturing example may not be significantly impacted by autonomous manufacturing; however, autonomous manufacturing has the potential to be transformative for manufacturing objectives in which the design space and fundamental process and artifact physics are not as well understood and thus evade traditional manufacturing design. Consider the objective of 3D metamaterial manufacture with a specified transmission spectrum, such as the metamaterial problem studied here. This application has a 3D design space and the critical engineering variable of strain propagates in 3D [2-4]. Two-dimensional and 3D metamaterials are often analyzed with 2D and 3D computational analyses, evading simple design rules. Furthermore, manufacturing inaccuracies and incorrect model assumptions result in discrepancies between the predicted and actual part performance [5], limiting the effectiveness of computational model-based topology optimization algorithms. Applications with similar engineering and manufacturing challenges include e-beam lithography [6], dielectric meta-surfaces [7], structural metamaterials [8], and soft robotics [9]. The objective of this work is related to a few different automated and autonomous manufacturing systems that automatically generate experiments and test product properties. These include the autonomous discovery of new drug compounds [10,11], single-walled carbon nanotubes [12], and photocatalyst mixtures for improving the efficiency of hydrogen production [13]. These systems are part of a larger manufacturing community effort to integrate ML into manufacturing analysis and operation [14-16].

This work is a proof-of-concept study of autonomous manufacturing with the specific objective to manufacture a phononic crystal (PnC). PnCs are a class of acoustic metamaterial in which the design of periodic elements controls the bandpass of the transmission of ultrasonic elastic waves, with a user-defined bandpass specification. The system, entitled the autonomous manufacturing system for phononic crystals (AMSPnC), is composed of additive manufacturing (AM), part transport, part testing, and cognition elements (Fig. 1). The system takes raw materials and user-defined performance specifications as inputs and autonomously prints and then tests part performance, either in batch or with new updated process parameters at each print. The outputs are the artifacts, qualified material performance for each artifact, and knowledge of the empirical physical relationships between design parameters and performance. For this specific case study, we employ supervised learning methods [17] to generate an empirical model of the collected dataset \mathcal{D} and then apply standard optimization algorithms to generate a parameter set to attain user-defined specifications. The AMSPnC system has a customizable cognition element such that supervised learning, reinforcement learning, and optimization algorithms can be efficiently applied and tested. Critically, the system exhibits the standard challenges of a manufacturing system—parameter resolution limits, raw material uncertainty, process uncertainty and probabilistic failure, process operating window limits, and measurement noise and uncertainty—and thus provides a realistic testbed for prototyping more sophisticated cognition element designs. Of course, the diversity in manufacturing processes is large and the AMSPnC cannot capture all manufacturing challenges in a single system; potentially, the AMSPnC design can motivate similar autonomous manufacturing efforts on other classes of manufacturing systems. Regardless, to the best of our knowledge, this is one of the first attempts at ML systems integration for autonomous manufacturing of a 3D part, whereas recent studies have only explored 2D geometries such as 3D printing of simple lines [18,19].

The remainder of the paper is organized as follows. Section 2 provides a systems representation of the manufacturing problem and provides background on PnCs. Section 3 details the AMSPnC design. Section 4 details a case study applied to the AMSPnC and Sec. 5 provides the corresponding results. Section 6 provides interpretations of the current study and the direction of the future study.

2 Background

2.1 Manufacturing System Representation and Performance Metric. Consider the general manufacturing process \mathcal{F} :

$$\mathbf{g}_t = \mathcal{F}(\mathbf{x}_t) + \boldsymbol{\xi}_t \tag{1}$$

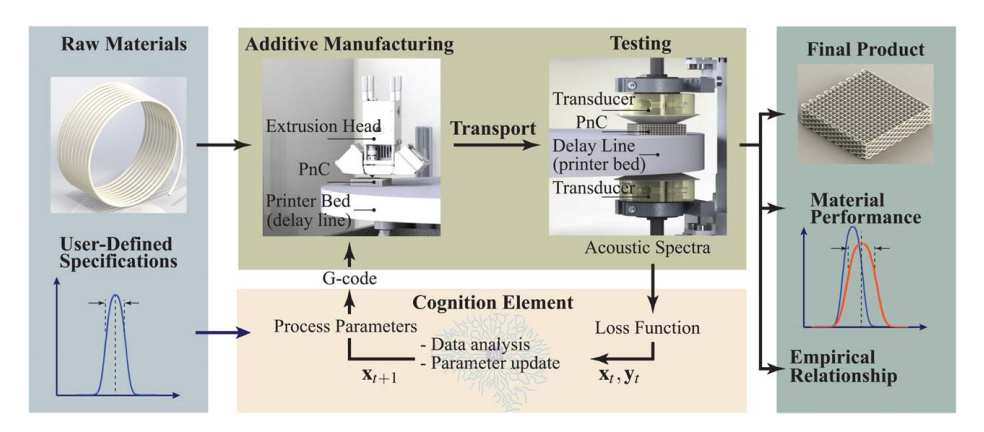


Fig. 1 Schematic of the AMSPnC ("Extrusion Head" by thinkin3D is licensed under CC BY-NC 3.0)

where the process output $\mathbf{g}_t \in \mathbb{R}^m$ quantifies the part property or properties, the process input $\mathbf{x}_t \in \mathbb{R}^n$ quantifies manufacturing parameters, $\boldsymbol{\xi}_t$ is the process noise, t is the trial index, and T is the total number of trials:

$$\mathbf{x}_{t} = [x_{t,1}, x_{t,2}, \dots, x_{t,n}]'$$

$$\mathbf{g}_{t} = [g_{t,1}, g_{t,2}, \dots, g_{t,m}]'$$

$$t \in [0, 1, \dots, T]$$

where \prime denotes the transpose operator. For a desired output specification \mathbf{g}_d , the objective of the learning problem is to find optimal design parameters \mathbf{x}^* , subject to the constraint $\underline{\mathbf{x}} \leq \mathbf{x}^* \leq \overline{\mathbf{x}}$, which minimizes a loss function $\mathbf{y} = \mathcal{L}(\mathbf{g}_d, \mathbf{g}_i)$ that quantifies the deviation between the \mathbf{g}_d and \mathbf{g}_i . The \leq symbol denotes the element-wise inequality: $\mathbf{x}_1 \leq \mathbf{x}_2 \leftrightarrow [\mathbf{x}_1]_i \leq [\mathbf{x}_2]_i, \forall i$. $\underline{\mathbf{x}}$ is a vector of the minimal allowable parameter values and $\overline{\mathbf{x}}$ is a vector of the maximum allowable parameter values. The loss function is a generic term for a weighted function of performance metrics, in which many methods have been devised to quantify performance and enforce constraints [20,21].

2.2 Acoustic Metamaterials (Phononic Crystals). PnCs are a class of acoustic metamaterials in which the transmission spectra of the elastic waves are dependent on the periodic structure of the material [22]. For instance, wave propagation in the Z direction of a representative PnC in Fig. 2(a) is dependent on the design of the filament diameter (d) and the filament-to-filament distance (l_{xy}) (Fig. 2(b)). In this study, we characterize the performance of a PnC by its frequency, f, dependent transmission spectra |T(f)|, defined as the ratio of the output spectra to the input spectra. The objective is to manufacture a PnC with the specified acoustic bandpass. The performance metrics are the bandpass center frequency, f_c , and bandwidth, w: $\mathbf{g} = [f_c, w]'$. A schematic of the test method

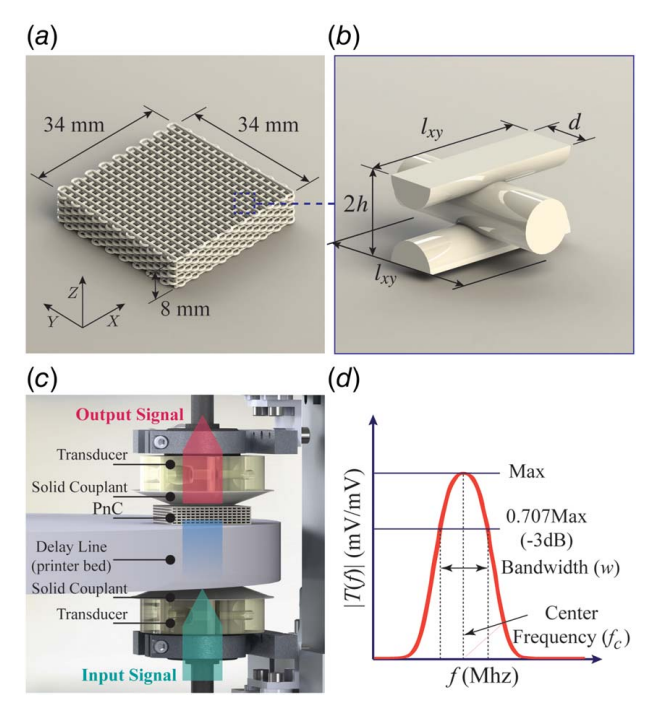


Fig. 2 Representative PnC and ultrasonic testing: (a) Schematic of an acoustic metamaterial (PnC). (b) Unit cell of a PnC and annotated design parameters d and l_{xy} . (c) Schematic of the transmission of an elastic wave from the bottom ultrasonic transducer to the top ultrasonic transducer through a bottom solid couplant, delay line, PnC, and then a top solid couplant. (d) Idealized transmission spectra demonstrating a phononic bandpass and bandpass metrics.

to measure |T(f)| is shown in Fig. 2(c) and an idealized transmission spectrum with annotated performance metrics is shown in Fig. 2(d).

3 System Design

The AMSPnC consists of four main subsystems: AM, transport, testing, and cognition. A computer-aided design (CAD) rendering of AMSPnC with detailed hardware subsystems is shown in Fig. 3(a). A photo of the AMSPnC is shown in Fig. 3(b).

3.1 Additive Manufacturing Subsystem. A consumer-grade fused filament fabrication (FFF) 3D printer (Ultimaker S5, Ultimaker, Utrecht, Netherlands) was adapted as the AM subsystem. The AM subsystem is largely used as received, with the main modifications being the removal of printing substrate to attach the transport subsystem (Sec. 3.2) and the mounting of the testing subsystem (Sec. 3.3). The delay line of the transport subsystem serves as the printer bed for the AM subsystem. The printing head location is defined by coordinate triad $\{X, Y, Z\}$ and material extrusion is defined by coordinate E. All PnCs are printed at the same $\{X, Y, Z\}$ start point (Fig. 4).

3.2 Transport Subsystem. The transport subsystem is designed to deliver an unoccupied location on the printer bed (delay line) to the printing location for PnC manufacturing and deliver a manufactured PnC to the testing location. The transport subsystem coordinate is given by rotation θ (Fig. 4). The motor is mounted to the *Z*-axis stage and the delay line (printer bed) is mounted to the motor (DC-micromotor, Series 3257G024CR, Schönaich, Germany with encoder, HEDS-5500, Broadcom Inc, CA, USA).

3.3 Testing Subsystem. The ultrasonic testing subsystem measures the transmission spectra of a PnC artifact by sending an

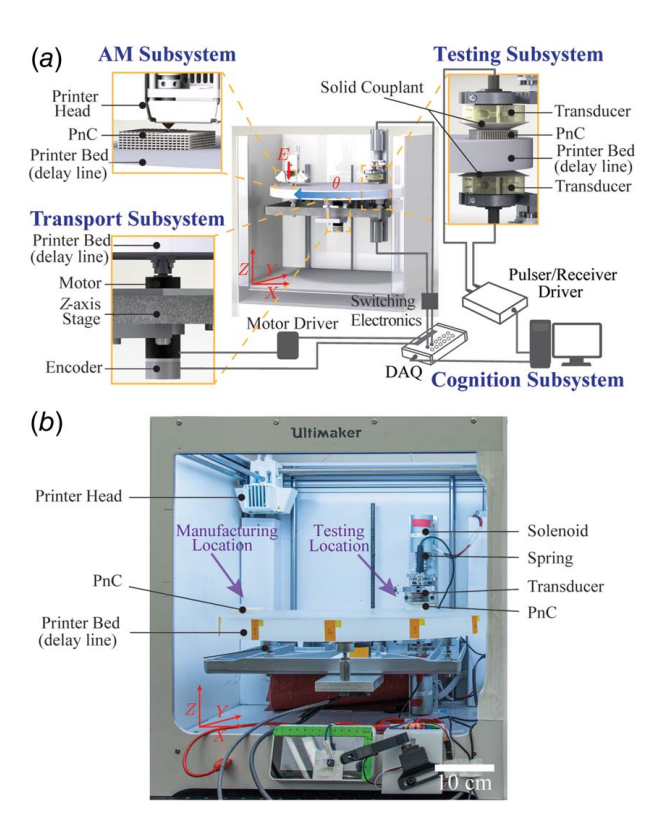


Fig. 3 AMSPnC: (a) rendered CAD model of the AMSPnC, highlighting the four main subsystems, and (b) photograph of the AMSPnC

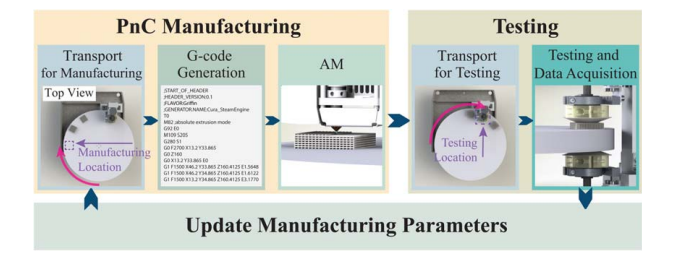


Fig. 4 Detailed workflow for each trial of the automated training set execution task

ultrasonic pulse from the pulser (bottom) transducer and then through the bottom couplant, delay line, PnC, and top couplant to the receiver (top) transducer (Fig. 2(c)). The following sequence is used for each ultrasonic test: the transport subsystem moves a PnC artifact into the testing subsystem; the top and bottom solenoids disengage, causing two spring loaded ultrasonic transducers (A105S-SB Olympus, Tokyo, Japan) to clamp the PnC artifact from the top and delay line from the bottom; an ultrasonic pulse is sent to the bottom transducer and received by the top transducer (USBUT350, US Ultratek Inc, CA, USA); additional pulses at different center frequencies are sent to the bottom transducer according to the testing scheme detailed in Sec. 3.4.5; the top and bottom solenoids are engaged to release the transport subsystem and end the test. The ultrasonic delay line (Rexolite® Polystyrene, C-Lec Plastics Inc, PA, USA) temporally separates the primary transmission signal from the reflections at impedance mismatched interfaces [2]. A solid couplant (AqualinkTM100, Innovation Polymers, Canada) is adhered at the edges to a 3D printed transducer holder, which ensures that the couplant is free on the transducer surface, but taut so that the couplant does not wrinkle. The entire subsystem is mounted to the Z-stage of the AM subsystem. The two transducers in our system have a center frequency of the transducer bandpass specification of 2.25 MHz.

3.4 Cognition Subsystem. The objective of the cognition subsystem is to automatically test a set of PnC design parameters l_{xy} and d and then autonomously select optimal design parameters l_{xy}^* and d^* to achieve a desired PnC performance. This objective sets up the optimization problem

$$\min_{\mathbf{x}_{t}} \mathbb{E}[\mathcal{L}(\mathbf{g}_{d}, \underbrace{\mathcal{F}(\mathbf{x}_{t}) + \xi_{t}}_{\mathbf{g}_{t}}]$$
s.t. $\underline{\mathbf{x}} \preceq \mathbf{x}_{t} \preceq \overline{\mathbf{x}}$ (2)
$$\mathbf{x}_{t} = \begin{bmatrix} x_{t,1}, x_{t,2}, \dots, x_{t,n} \end{bmatrix}'$$

$$t \in [0, 1, \dots, T]$$

The cognition subsystem in Fig. 1 is designed to find the optimal \mathbf{x}^* by empirically testing the process function \mathcal{F} in either batch testing or serial testing. This paper investigates batch testing as a proof of concept; however, other works by our lab have investigated serial testing, as discussed in Sec. 6 [23]. The coordination of these empirical testing and optimal parameter selection requires a multitude of scheduled tasks, which are detailed below. All functions are integrated into the main LABVIEW program (National Instruments, Austin, TX, USA). The general information flow is shown in Fig. 5.

3.4.1 Cognition Element. The cognition element generates an empirical model that discovers the underlying relationship within dataset \mathcal{D} and then finds an optimal parameter set $\mathbf{x}^* = \begin{bmatrix} l_{xy}^*, d^* \end{bmatrix}'$ to attain a user-defined specification using standard optimization algorithms. A case study of a specific cognition element design is provided in Sec. 4.2.

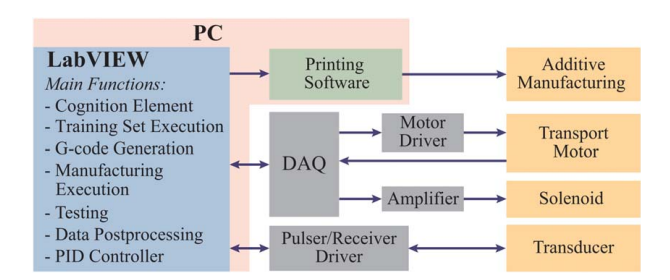


Fig. 5 Information flow diagram for AMSPnC. Commands flow from the LABVIEW program to the printer software, auxiliary hardware, and actuators and sensors.

- 3.4.2 Training Set Execution. The training set to generate dataset \mathcal{D} is built by a scheduled set of manufacturing and testing operations. This schedule is automatically executed, with each manufacturing and testing operation executed in the loop shown in Fig. 4: transport, G-code generation, AM, transport, and testing.
- 3.4.3 G-Code Generation. A custom-built G-code generator prescribes the AM printing path based on a given d and l_{xy} design.
- 3.4.4 Manufacturing Execution. The AM subsystem executes PnC manufacturing with G-code commands sent from 3D slicer software, cura (Ultimaker, Utrecht, Netherlands), via an ethernet port. cura loads and sends G-code via a batch script in LABVIEW.
- 3.4.5 Testing. The testing subsystem conducts ultrasonic testing of each manufactured PnC. The test consists of multiple applications of the tone burst signal by the bottom transducer, each at a different fundamental excitation frequency f_0 :

$$v(t) = A\cos(2\pi f_0 t) \left(\frac{1}{2} + \frac{1}{2}\cos\left(\frac{2\pi f_0}{M}t\right)\right) \operatorname{rect}\left(\frac{M}{2f_0}\right)$$
(3)

where A is the voltage amplitude, M is the number of fundamental periods in the tone burst, and rect is the zero-phase rectangular function [24]. A single tone burst signal provides broadband excitation of the system with a bandwidth of $1.441(f_0/M)$, while being brief in duration such that the signal is transmitted before the measurement is polluted by reflections at impedance mismatched interfaces.

3.4.6 Data Processing. A custom matlab script in labview performs data post-processing operations: merge multiple tests at different excitation frequencies, transmission spectra calculation, assess bandpass metrics, and generate dataset $\mathcal{D} = \{\mathbf{x}, \mathbf{y}\}$ for the cognition element.

4 A Case Study

A case study is performed to demonstrate the concept of autonomous manufacturing to satisfy a performance specification. The training set $\mathcal{D} = \{\mathbf{x}, \mathbf{y}\}$ is built via automated progression through a full-factorial DoE with three replicates. The cognition element is based on the supervised learning algorithm polynomial regression, which fits an empirical relationship between design parameters and a loss function composed of the PnC transmission metrics of center frequency f_c and bandwidth w. After training, a function minimization algorithm, differential evolution, is applied for three different desired center frequency/bandwidth pairs and then five independent PnC manufacturing and testing operations are performed to validate the method and algorithm performance.

4.1 Training Set Development

4.1.1 Automated Procedure. There are 12 predefined printing locations on the surface of the printing bed, each offset by

30 deg. The printing location and testing location are fixed at a 106.2 deg offset (Fig. 4). The sequence of automation is described in Algorithm 1.

4.1.2 Full-Factorial Design of Experiment. A full-factorial DoE is performed to generate dataset $\mathcal{D} = \{\mathbf{x}, \mathbf{y}\}$. The PnCs are fabricated with discrete filament diameters, d, and filament-to-filament distance, l_{xy} , design levels,

$$d = 350, 400, \dots, 600 \,\mu\text{m}$$

$$l_{xy} = 700, 750, \dots, 1050 \,\mu\text{m}$$
 (4)

for a total of 48 unique combinations. The levels above are based on those reported in the literature [2]. The DoE uses three replicates for a total of 144 PnCs and the manufacturing order is randomized. With 12 available manufacturing locations on the surface of the transport subsystem bed, manufacturing is completed in 12 sets.

4.1.3 Manufacture of Phononic Crystals. Polylactic acid filament (Ultimaker) with a diameter of 2.85 mm and a glass transition temperature of approximately 60 °C is selected as the raw material due to the ease of fabrication and relatively low glass transition temperature. PnCs are manufactured on the surface of the transport subsystem with the printing specifications given in Table 1. A uniform speed is used to ensure a consistent PnC filament diameter, which improves transmission amplitude of the PnC. A representative PnC is shown in Fig. 2(a). Support structures are not required and not used for the PnC design used herein.

The extrusion feed per nozzle distance traversed (dE/dL) is set in G-code to be

$$\frac{\mathrm{d}E}{\mathrm{d}L} = \frac{4dh}{\pi D^2} \tag{5}$$

where D is the diameter of the raw material filament, d is the desired filament diameter of the PnC, h is the height of each layer, and h = d in this study.

The printer head starts at the same location $\{X, Y\}$ for each PnC manufacture. The Z position is offset by a calibration constant, calibrated by a flatness measurement using a dial gauge at each location on the transport subsystem. A manufacturing batch takes approximately 5–6 h, depending on the design levels of the PnCs in the set.

4.1.4 Testing. Ultrasonic testing consists of two basic measurements: reference transmission measurement and PnC transmission measurement. The reference transmission measurement is the measurement of the receiving (top) transducer voltage, $V_r(t)$, when there is an ideal transmitter between the transducers. We emulate an ideal transmitter by placing a reference sample of the same size as the PnC but composed of the same material as the delay line, polystyrene. Two reference measurements using two identically constructed reference samples are collected at a randomized location before each manufacturing set. A thin layer of ultrasound transmission gel (Aquasonic 100, Parker Laboratories, NJ, USA) is applied between the delay line and reference sample to ensure ideal transmission. PnC transmission is measured by the receiving transducer voltage, $V_{\rm PnC}(t)$, when there is a PnC artifact between the transducers. The sequence of operations is described in Sec. 4.1.1. The PnC polymer elastic modulus is temperature

Table 1 Manufacturing parameters

Nozzle temperature	205 °C
Nozzle diameter	0.4 mm
Printing speed	1500 mm/min
Dimension of PnCs	$34 \text{ mm} \times 34 \text{ mm} \times 8 \text{ mm}$
Layer height (layer 1)	$\frac{3}{4}d$
Layer height (layer >1)	d
Filament stacking orientation	Orthogonal

dependent and thus the transmission spectra is temperature dependent [25]. Accordingly, the testing scheduling logic in Algorithm 1 ensures that each PnC cools for 20 min after manufacturing to ensure full polymer crystallization.

Algorithm 1 Automated procedure for training set generation for each batch of 12 PnCs

1: **Manual setup.** This step is only performed at printing location i = 1 at the beginning of every 12 PnCs.

Conduct reference signal tests with reference samples. See Section 4.1.4.

Position the bed into the first fabrication location.

i = 1.

2: **While** $i \le 12$ **do**

3: Transport to PnC fabrication location

Activate solenoids to free the rotation of transport subsystem. Rotate the transport subsystem to 30(i-1) deg.

4: Generate G-code

Deactivate solenoids to lock the transport subsystem.

Access design parameters (d, l_{xy}) .

Generate and save G-code to a file.

5: Manufacture PnC

Load the G-code file with CURA and send to the 3D printer. Execute PnC manufacture.

6: Transport to testing location

IF i = 1; GOTO Step 8.

ELSEIF i < 12

Activate solenoids to free the rotation of transport subsystem bed.

Transport the previously printed PnC to the test location: $\theta = (106.2 + 30(i - 1))$ deg.

ELSE

Wait for 20min to cool down the PnC (Sec. 4.1.4).

Activate solenoids to free the rotation of transport subsystem bed.

Transport the current PnC to the test location: $\theta = (106.2 + 30i)$ deg.

7: Test PnC artifact

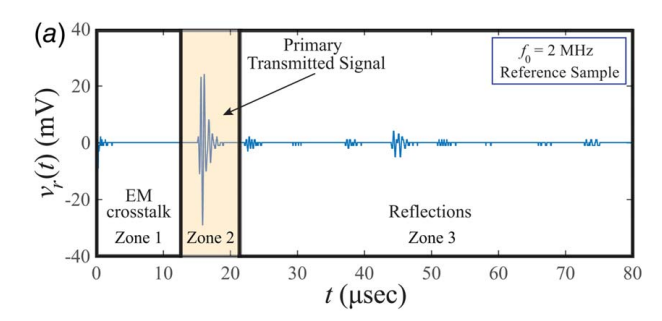
Deactivate the solenoids to clamp the PnC with the transducers. Test the PnC with a sequence of five tone burst signals at different center frequencies (Sec. (Sec. 3.4 and Appendix A.1). Postprocess data. Add data pair $\{x,y\}$ to data set D.

8: **Increment** i = i + 1

9: **end**

The actuation signal is a temporally separated sequence of tone burst signals, where each tone burst is of the form of Eq. (3) (shown in Fig. 6(a)). Here, we execute a sequence of tone burst signals with $f_0 = 1$, 1.5, 2, 2.75, 4 MHz and then merge the responses using the algorithm described in Appendix A.1 to further expand the frequency band of excitation to improve the signal-to-noise ratio at the low and high frequencies. Both the reference and PnC transmission measurements are sampled at 50 MHz.

4.1.5 Data Processing. Figure 6 shows representative waveforms of the reference transmission measurement, $v_r(t)$, and the PnC transmission measurement, $v_{PnC}(t)$, for a tone burst input with $f_0 = 2$ MHz. The waveforms show the temporal separation between the primary transmitted signal and the reflections from impedance mismatches at material interfaces. Additionally, there is electromagnetic crosstalk between the pulser unit and receiver unit from the initial pulse. The primary transmitted signal is segmented as shown in Fig. 6 (562 samples for $v_r(t)$ and 1502 samples for $v_{PnC}(t)$) and then zero padded to length 4000 to achieve the desired frequency resolution of 0.0125 MHz. The Blackman window [26] is applied to the segmented and zero-padded signals. The five different measurements for the five



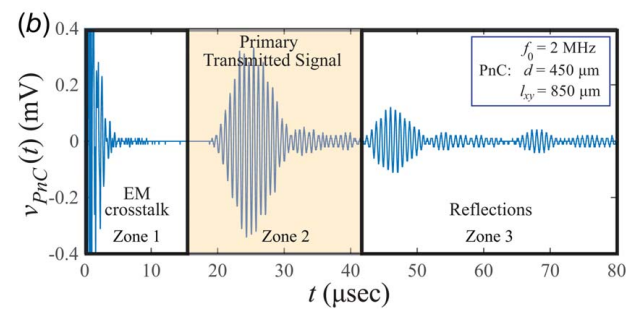


Fig. 6 Representative time-domain waveforms of the transmission measurement signals: (a) transmitted reference signal, $v_r(t)$ and (b) transmitted PnC signal, $v_{PnC}(t)$

Table 2 Desired transmission metrics

Pair no.	$f_{c,d}$ (MHz)	w_d (MHz)		
1	0.63	0.15		
2	1.20	0.13		
3	0.48	0.09		

different f_0 levels are combined to compute a single transmission spectra of the PnC, |T(f)||; each signal is transformed to the frequency domain, filtered with a frequency localizing basis function, and merged in the frequency domain. The metrics of center

frequency (f_c) and bandwidth (w) are identified from |T(f)|| by fitting a bimodal Gaussian function to |T(f)||. The algorithm for multiple excitation frequency merging and then metric identification are detailed in Appendix A.2.

4.2 Cognition Element

4.2.1 Loss Function. Given the performance metrics of center frequency f_c and bandwidth w (Fig. 2(d)), a loss function is defined to penalize deviation from desired performance:

$$\mathcal{L}(\mathbf{y}_d, \mathbf{y}_a) = \alpha \mathcal{L}_f + \mathcal{L}_w \tag{6}$$

where

$$\mathcal{L}_f = \frac{\left| f_{c,a} - f_{c,d} \right|}{f_{c,d}}$$

$$\mathcal{L}_w = \frac{\left| w_a - w_d \right|}{w_d}$$

Loss component \mathcal{L}_f is the normalized difference between the actual center frequency, $f_{c,a}$, and desired center frequency, $f_{c,d}$. Loss component \mathcal{L}_w is the normalized difference between actual bandwidth, w_a , and desired bandwidth, w_d . A representative desired transmission spectra are shown in Fig. 2(d). \mathcal{L}_f coefficient α weights the relative penalty for center frequency deviation and bandwidth deviation, with a higher coefficient more heavily penalizing frequency deviation. In this case study, three loss functions are tested (loss functions 1, 2, and 3), with α chosen to be 1, 2, and 4, respectively; the choice of $\alpha \geq 1$ for all loss functions reflects that bandpass filters are often primarily defined by their center frequency.

4.2.2 Polynomial Regression. As defined in Eq. (1), the input parameter set is $\mathbf{x} = [d, l_{xy}]'$ and the output set is $\mathbf{g} = [f_c, w]'$. The goal is to find the optimal d^* and l_{xy}^* of PnC such that the loss value, $\mathbf{y} = \mathcal{L}^*$, is minimal based on given performance specifications $\mathbf{g}_d = [f_{c,d}, w_d]'$. The supervised learning method polynomial regression is applied to learn from 144 experimental dataset pairs, $\mathcal{D} = \{\mathbf{x}, \mathbf{y}\}, \mathbf{x} \in \mathbb{R}^{144 \times 2}, \mathbf{y} \in \mathbb{R}^{144 \times 1}$, to generate a loss surface. To train and test the model, the dataset \mathcal{D} is split into training data

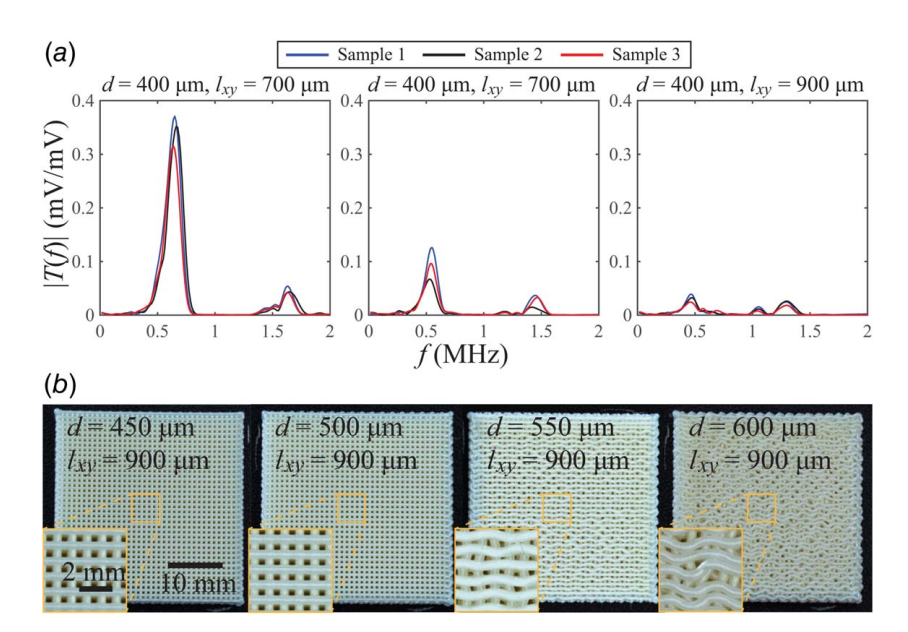


Fig. 7 Representative transmission spectra and artifacts from the training data set. (a) Transmission spectra at three representative d, l_{xy} pairs. The center frequency decreases as the filament-to-filament distance increases. (b) Images of printed PnCs from the training set. As the filament diameter d increases above 550 μ m, a buckling phenomenon emerges that disrupts PnC periodicity.

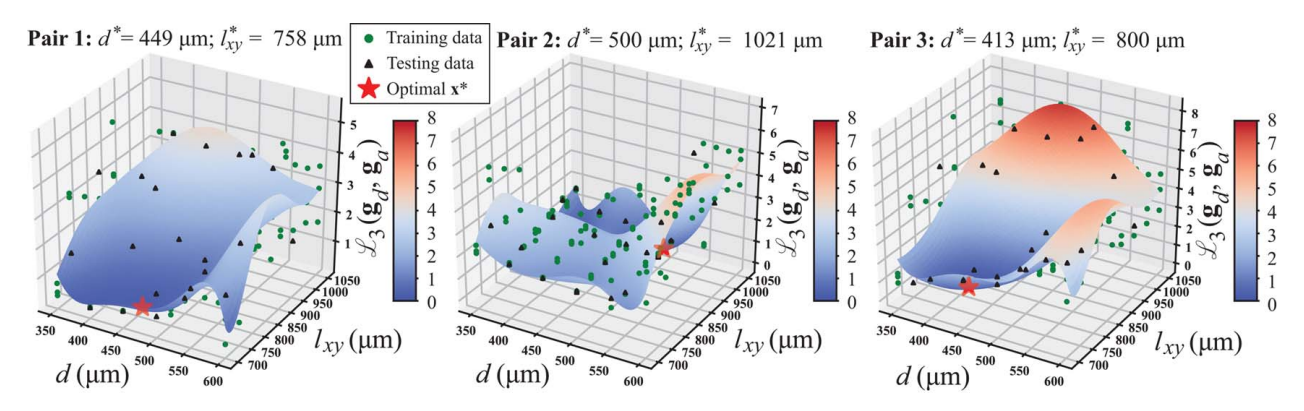


Fig. 8 Supervised learning results for loss function 3, \mathcal{L}_3 , for each of the transmission metrics pairs. Resultant optimal parameters are indicated on the surface for three pairs.

Table 3 Training and testing error (MSE)

	Loss function 1		Loss fu	nction 2	Loss function 3		
Pair	$arepsilon_{TR}$	$arepsilon_{TE}$	$arepsilon_{TR}$	$arepsilon_{TE}$	$arepsilon_{TR}$	$arepsilon_{TE}$	
1	0.45	0.57	0.52	0.61	0.77	0.73	
2	0.58	0.79	0.64	0.90	0.79	1.13	
3	0.83	1.00	0.95	0.92	1.40	0.99	

and testing data with a 85%:15% split, respectively. Ten-fold cross-validation is used to prevent overfitting and select the best polynomial degree between 0 and 21 [27]. The training error and testing error of the polynomial regression model are defined as ε_{TR} and ε_{TE} , respectively, based on the mean square error (MSE) in Eq. (7).

$$\varepsilon_{(\cdot)}(\mathcal{L}, \hat{\mathcal{L}}) = \frac{1}{N} \sum_{i=1}^{N} (\mathcal{L}_i - \hat{\mathcal{L}}_i)^2$$
(7)

where N is the total number of samples used to calculate the MSE and \mathcal{L} and $\hat{\mathcal{L}}$ are the actual loss and predicted loss, respectively.

4.2.3 Optimization Problem. The ultimate objective of the system is to autonomously identify a design parameter set that provides the minimum loss for desired transmission spectra metrics. This objective is stated as a minimization problem:

$$\{d^*, l_{xy}^*\} = \underset{d, l_{xy}}{\operatorname{argmin}} \ \mathbb{E}[\mathcal{L}(\mathbf{g}_d, \mathbf{g}(d, l_{xy}))] \tag{8}$$

such that

$$\begin{bmatrix} 350 \,\mu\text{m} \\ 700 \,\mu\text{m} \end{bmatrix} \leq \begin{bmatrix} d \\ l_{xy} \end{bmatrix}_t \leq \begin{bmatrix} 600 \,\mu\text{m} \\ 1050 \,\mu\text{m} \end{bmatrix}$$

The function minimization algorithm differential evolution [28] is applied to Eq. (8) to find the optimal d^* and l_{xy}^* with a minimal predicted loss, $\hat{\mathcal{L}}$.

4.3 Validation. To validate the approach outlined in Fig. 1, we randomly generated three desired center frequency/bandwidth pairs $(f_{c,d} \text{ and } w_d, \text{Table 2})$ from within the parameter range of the training set \mathcal{D} , calculated optimal input parameters d^* and l^*_{xy} , and then performed independent manufacturing and testing of these PnCs. The complete validation set includes the three different spectra metrics from Table 2, three different loss functions defined in Sec. 4.2.1, and five independent manufacturing and testing repetitions, for a total of 45 validation data points. Experimental loss and transmission spectra are reported for comparison.

Table 4 Optimal design parameters and loss

	Loss function 1			Loss function 2			Loss function 3		
Pair	d*	l_{xy}^*	\mathcal{L}_1^*	d*	l_{xy}^*	\mathcal{L}_2^*	d*	l_{xy}^*	\mathcal{L}_3^*
1	481	740	0.05	474	746	0.08	449	758	0.28
2	367	1050	-0.06	370	976	0.14	500	1021	0.22
3	448	787	-0.08	439	802	0.06	413	800	0.06

5 Results

Training Set Results. One hundred and forty-four PnCs were manufactured according to the schedule detailed in Sec. 4.1.2. Figure 7 displays representative results from a subset of the manufactured PnCs. In agreement with the literature [2], a consistent trend is that there is an inverse relationship between center frequency and filament-to-filament spacing, l_{xy} . The center frequency shifts from larger to smaller values as parameter l_{xy} shifts from smaller to larger values; a representative observation is the center frequency decreases from approximately 0.65 MHz to 0.46 MHz as l_{xy} increases from 700 μ m to 900 μ m at a constant d (400 μ m) (Fig. 7(a)). Filament diameter designs with d less than $550 \,\mu \text{m}$ yield straight, uniform filaments with a consistent periodicity (Fig. 7(b)). At larger filament diameter designs, the filaments buckle, breaking the periodicity in the structures. The lack of periodicity yields an artifact that does not act as a metamaterial, creating an all-reject filter in which the signal strength is significantly diminished across all frequencies (data not shown).

The computed loss using loss function \mathcal{L}_3 at the three desired transmission metrics in Table 2 for all 144 manufactured PnC artifacts are shown in Fig. 8; the loss values using \mathcal{L}_1 and \mathcal{L}_2 are shown in Fig. 13 of the Appendix. A loss surface is fit to each loss function using polynomial regression, Sec. 4.2.2, providing an estimate of the expected loss across the entire design space domain. Training error, ε_{TR} , and testing error, ε_{TE} , are dependent on the associated loss function and testing pair (Table 3); however, in general the testing error is slightly larger than the training error, and sometimes better than the training error, indicating an empirical model without appreciable overfitting. Additionally, the ramifications of a loss of structure periodicity from filament buckling, Fig. 7(b), are seen in the loss surfaces in Figs. 8 and 13; the highest loss values are associated with large filament diameters, hence buckling prone parameters, leading to severely attenuated transmission amplitudes and poor matching with the desired transmission performance.

5.2 Cognition Element and Validation Results. The set of optimal PnC designs, d^* and l_{xy}^* , for each loss function and transmission metric pair are given in Table 4 and superimposed on the

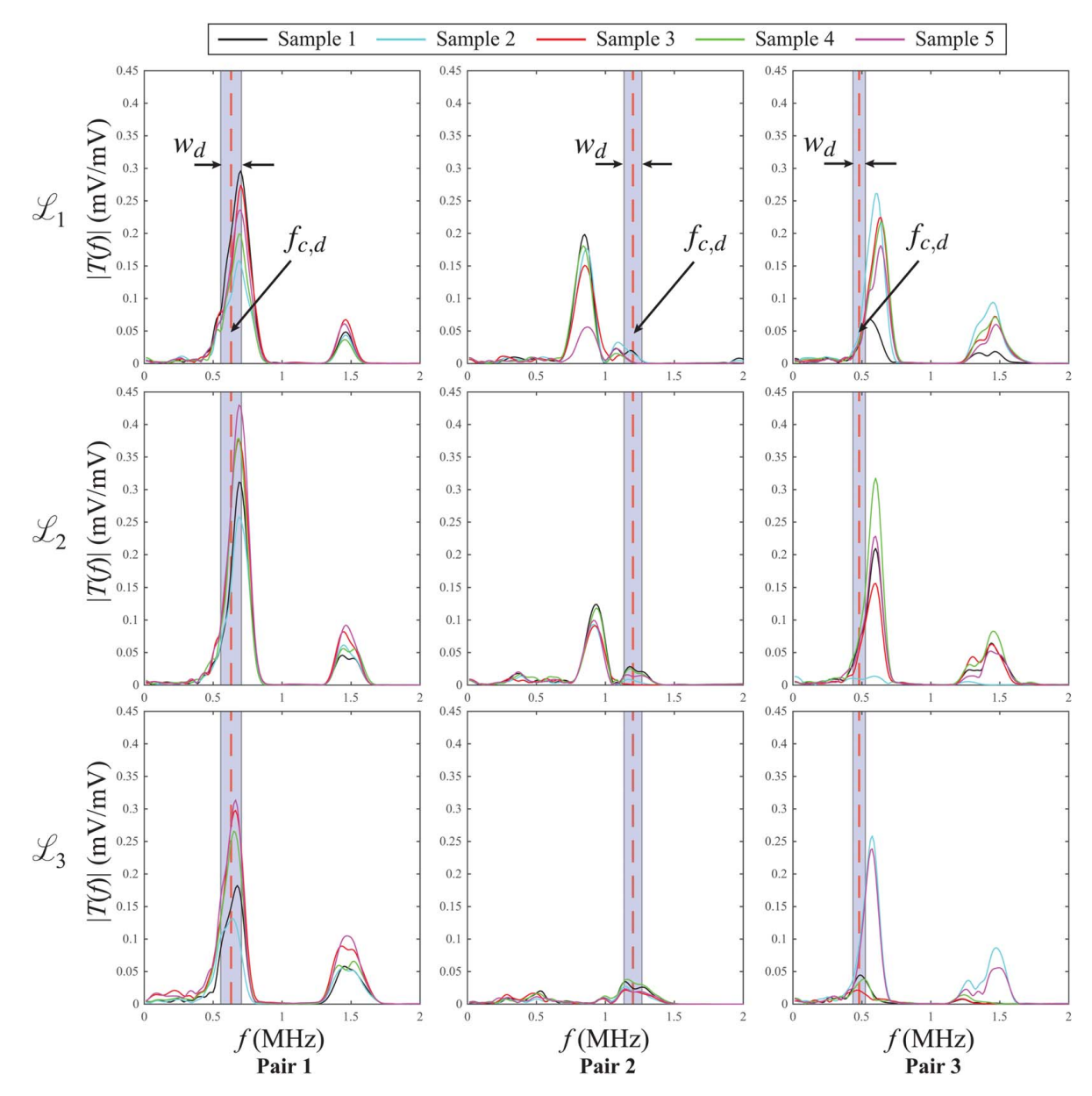


Fig. 9 Desired transmission parameters and validation results. Comparison of experimental transmission spectra for each sample and desired $f_{c,d}$ (dotted line) and w_d (gray shaded region) among the three loss functions.

Table 5 Tabulated validation results

$\mathcal{L}_{(\cdot)}$	Sample no.	Pair 1			Pair 2			Pair 3		
		$f_{c, \exp}$ (MHz)	w _{exp} (MHz)	$\mathcal{L}_{(\cdot),\mathrm{exp}}$	$f_{c,\exp}$ (MHz)	w _{exp} (MHz)	$\mathcal{L}_{(\cdot), exp}$	$f_{c,\exp}$ (MHz)	w _{exp} (MHz)	$\mathcal{L}_{(\cdot), exp}$
\mathcal{L}_1	1	0.69	0.13	0.19	0.84	0.09	0.57	0.56	0.11	0.42
•	2	0.68	0.15	0.09	0.85	0.09	0.57	0.60	0.10	0.38
	3	0.70	0.13	0.24	0.85	0.11	0.42	0.62	0.11	0.51
	4	0.68	0.13	0.21	0.84	0.10	0.54	0.63	0.11	0.52
	5	0.69	0.13	0.21	0.87	0.09	0.57	0.62	0.11	0.56
\mathcal{L}_2	1	0.69	0.11	0.46	0.93	0.10	0.66	0.59	0.10	0.62
	2	0.69	0.12	0.41	0.91	0.10	0.70	0.47	0.44	3.91
	3	0.68	0.12	0.38	0.92	0.11	0.65	0.58	0.10	0.58
	4	0.68	0.11	0.43	0.93	0.09	0.77	0.59	0.10	0.53
	5	0.69	0.11	0.41	0.91	0.10	0.71	0.59	0.10	0.56
\mathcal{L}_3	1	0.65	0.12	0.34	1.20	0.20	0.54	0.49	0.11	0.32
	2	0.62	0.13	0.20	1.19	0.18	0.45	0.57	0.10	0.79
	3	0.65	0.12	0.29	1.21	0.20	0.53	0.46	0.25	1.88
	4	0.64	0.12	0.27	1.21	0.20	0.54	0.50	0.12	0.50
	5	0.64	0.12	0.26	1.22	0.20	0.63	0.57	0.09	0.74

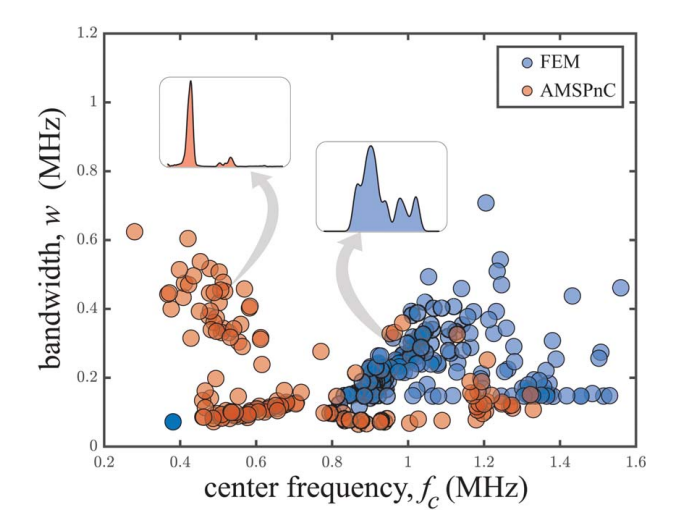


Fig. 10 Comparison of the process output metrics f_c and w for a computational model of a PnC (FEM) and experimental measurement by the AMSPnC. Two representative transmission spectra for the same input parameters d and l_{xy} show a distinctly different transmission spectra between FEM and experimental observation. ©2023 IEEE. Modified, with permission, from Ref. [30].

loss surfaces in Figs. 8 and 13. The results of manufacturing and testing optimal PnC designs for each loss function and testing pair are shown in Fig. 9. Qualitatively, more heavily penalizing a deviation in the center frequency metric forces the cognition element to choose a parameter design which yields a better compliance with the desired center frequency: compare \mathcal{L}_1 , which penalizes f_c and w deviation equally, with \mathcal{L}_3 , which penalizes f_c deviation four times stronger than w deviation (Fig. 9). Better center frequency compliance from \mathcal{L}_3 can be seen quantitatively in Table 5, as well. Anomalous manufacturing was observed in 1 of the 45 validation PnCs artifacts: sample 2, \mathcal{L}_2 , pair 3.

6 Discussion and Conclusion

The work here presents a new integrated manufacturing, testing, and cognition system, termed the AMSPnC, to test the concept of

autonomous manufacturing. The purpose of this testbed is to be a simple, inexpensive, and efficient method to test the cognition element of autonomous manufacturing systems. Although a simple system that is purpose driven for PnC manufacture, the AMSPnC has characteristics that are similar to those of high-value added manufacturing systems, such as those listed in the introduction, and is designed to be translatable to other manufacturing applications.

- The AMSPnC has a flexible design space and testing space. In the case study presented here, we chose a two-dimensional design space, $\mathbf{x} = [d, l_{xy}]'$, to limit the number of artifacts required in the training data set. However, the freeform nature of FFF manufacturing permits arbitrary structural designs, including non-orthogonal filament stacking and both intra- and inter-layer variation in d and l_{xy} , providing a rich exploration space for more sophisticated cognition algorithm development.
- Computational models of wave propagation through the PnC structure have model uncertainty, which will limit the effectiveness of zero-shot application of optimization and ML-based topology optimization algorithms. In a previous study from our group [29,30], we applied the acoustics module package of comsol to solve the elastic wave propagation problem by the finite element method (FEM) for all designs tested in this paper. Figure 10 shows the comparison between FEM and AMSPnC measured transmission metrics f_c and w for all printed samples; there is a marked difference in the distribution of these metrics, demonstrating uncertainty between model predictions and actual performance. The sensitivity of elastic wave propagation to the difficult to predict factors of necking at filament stacking interfaces, the material damping, and filament buckling during manufacturing (Fig. 7) highlight the importance of empirical learning in autonomous manufacturing, which innately captures these challenging factors. The flexible cognition element in the AMSPnC accommodates myriad ML-based algorithms, including those that merge computational models with empirical learning.
- The AMSPnC exhibits manufacturing relevant challenges which lead to imperfect data sets, some of which are not seen in computational studies, and thus provides a realistic emulation of advanced manufacturing processes for testing cognition algorithms. Anomalous manufacturing was

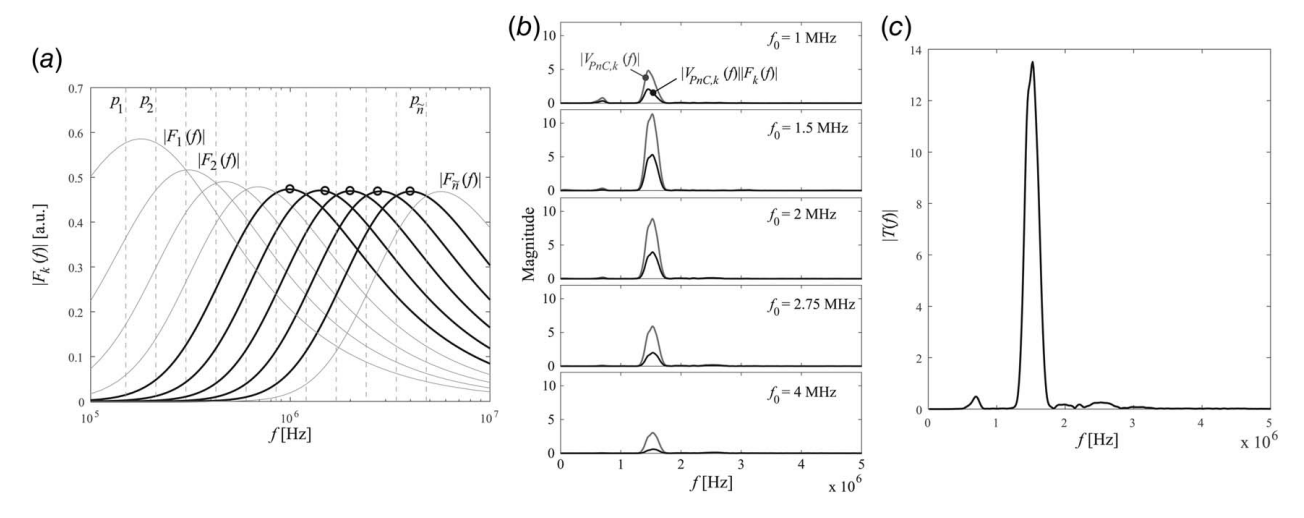


Fig. 11 Operations schematic demonstrating the methods of local tone burst weighting based on frequency localizing basis functions. (a) Magnitude of the frequency localizing basis functions $|F_k(f)|$, Eq. (A1). Circles denote the center frequency, f_0 , of ultrasound actuation. Gray functions denote unused functions in sequence from Eq. (A1). Black functions denote applied functions from Eq. (A1). Applied basis functions have the same peak magnitude and bandwidth. (b) Representative set of frequency domain responses before $|V_{\text{PnC},k}(f)||$ and after $|V_{\text{PnC},k}(f)||F_k(f)||$ weighting by frequency localizing basis functions. (c) Composite transmission spectra |T(f)|.

observed in one of the 45 artifacts in the validation sets, as defined by the loss being categorized as an outlier, in comparison to replications of the same design parameters or nearest neighbors in the training set. Statistical outliers are a common manufacturing challenge and developed autonomous manufacturing systems must be robust to them. Certain regions of the design space yield consistent manufacturing defects in the form of filament buckling (Fig. 7(b)); these features are common in advanced manufacturing where features such as thin walls and deep draws have a higher probability of manufacturing failure, and thus become unfavorable design features, probabilistically. Additionally, there are certain performance specifications that are not obtainable, providing a relevant material and design constraint on the expected performance. For instance, a center frequency greater than 1 MHz is difficult to achieve with the selected

- design space and materials; although heavily weighting the deviation in center frequency permitted us to identify a parameter set that achieved a bandpass at $1.20\,\mathrm{MHz}$ (Fig. 9, \mathcal{L}_3 , pair 2), the bandpass magnitude is weak in comparison to the bandpass magnitude achieved at lower frequencies.
- One of the fundamental components of any cognition element, the loss function, is tunable, providing a direct mechanism to weight specific performance metrics for the system. This influence can be best seen in Fig. 9 where a loss function that heavily penalizes deviations from the center frequency, L₃, leads to better compliance with the center frequency specification, in comparison to L₁ and L₂. This observed result gives promise for more sophisticated loss functions, such as loss functions that integrate pareto optimization or constraints [20,21] in future work.

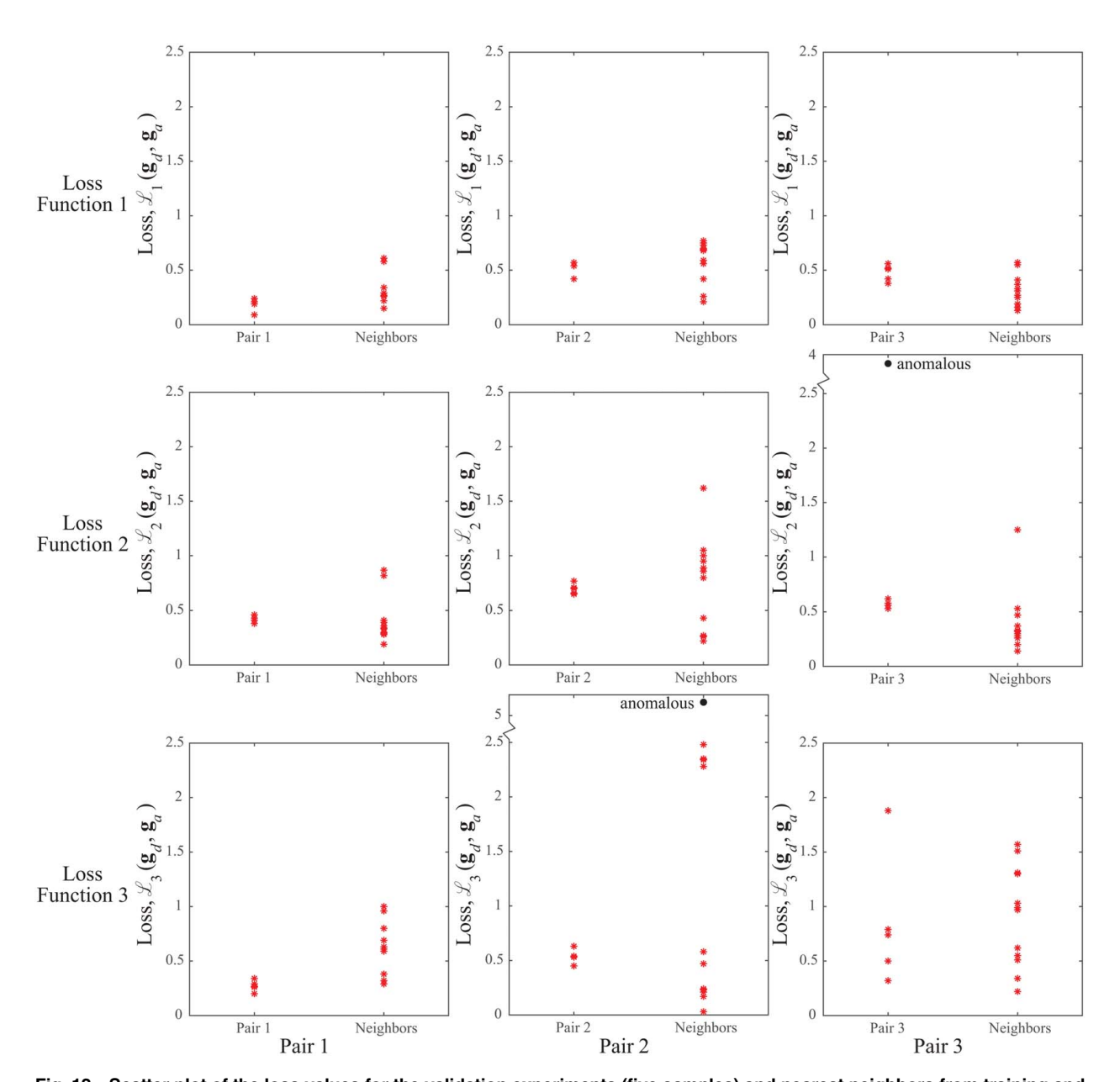


Fig. 12 Scatter plot of the loss values for the validation experiments (five samples) and nearest neighbors from training and testing sets (12 samples). Anomalous artifacts in the validation experiments are determined by the standard definition of an outlier. Anomalous artifacts in the nearest neighbors sets are defined by observation and qualitative investigation of the transmission spectra; only three replications are performed in the training set and testing sets that compose the nearest neighbors, precluding the standard statistical determination of outliers.

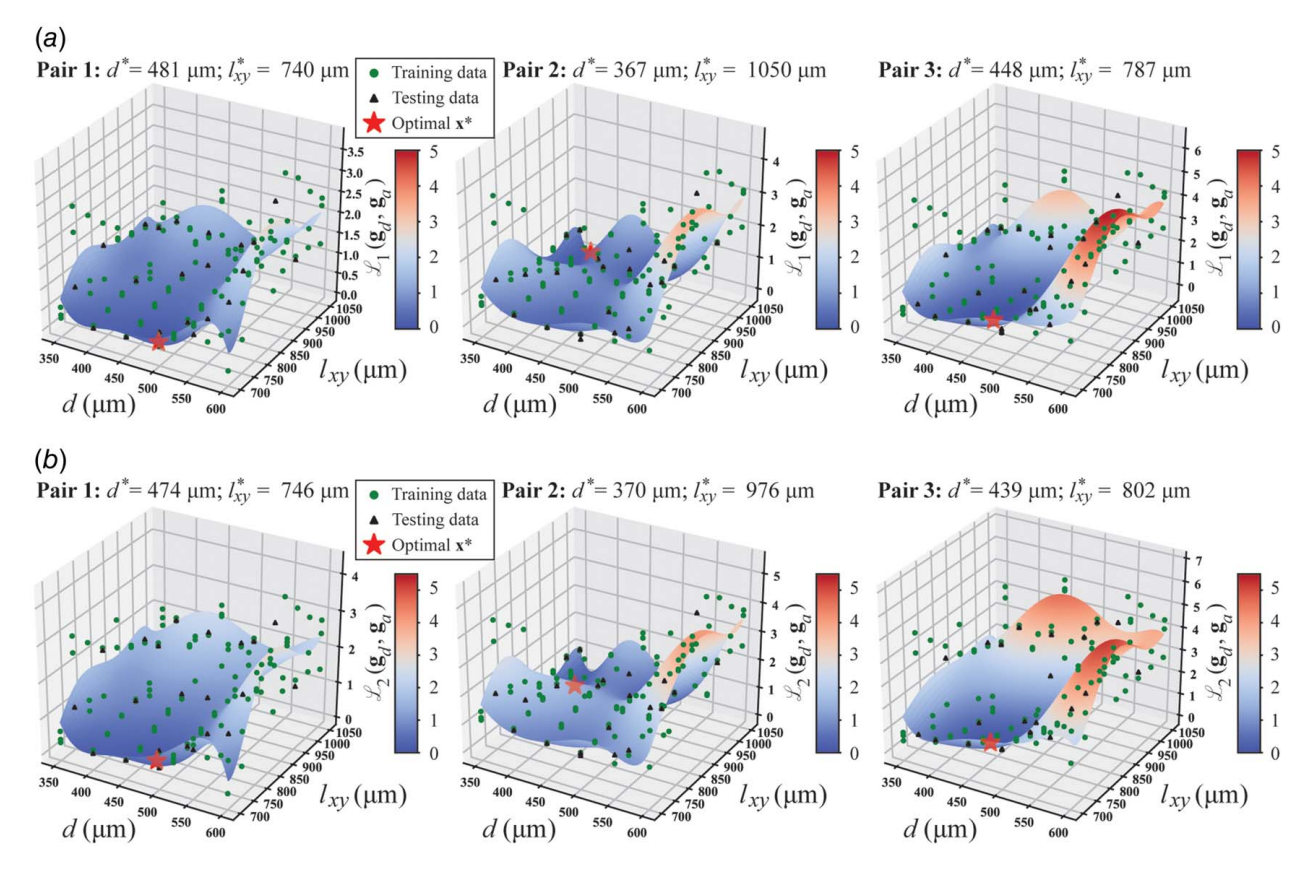


Fig. 13 Supervised learning results for loss functions 1 and 2, \mathcal{L}_1 and \mathcal{L}_2 , for each of the transmission metrics pairs. Resultant optimal parameters are indicated on the surface for three pairs.

The polynomial regression algorithm and function minimization scheme applied in the case study are simple options for the cognition element for a first, proof-of-concept case study to demonstrate some of the most basic properties of the AMSPnC. However, the true value of the AMSPnC is the ability to efficiently test myriad more advanced cognition element designs. A typical manufacturing process is expensive in terms of machine time, materials, and labor. To be machine time, materials, and labor efficient, ML algorithms embedded in the cognition element will need to converge to an optimal parameter set on the order of 10 samples, be robust to the inevitable anomalous manufacturing events, and be continuously applied, permitting the system to auto-regulate for deviations in material feedstock and environmental conditions. To do so, ML algorithms may integrate process and artifact physics models to reduce the need for large data sets, such as the ML algorithms previously explored by our group [29]. Unlike the serial process of training set development and then process optimization employed here, continuous, sequential ML algorithms, such as reinforcement learning [23], may be better suited to continually adapt to a changing environment or material and more tightly cluster empirical sampling near the optimal inputs l_{xy}^* and d^* for higher performance. Additionally, potential AMSPnC advancements could integrate other sensors, such as machine vision systems to measure actual filament spacing and diameter, $l_{xv,a}$ and d_a during the process to teach ML models the process-structure-performance relationship for the AMSPnC: commanded l_{xy} and d is the process input, measured $l_{xy,a}$ and d_a are the structure metrics, and measured $f_{c,a}$ and w_a are the performance metrics. Lastly, the design of the AMSPnC is most relevant to FFF 3D printing, but the concepts of having a flexible input space, online measurement, and flexible autonomous cognition and automated systems for communication are transferable design elements that may have impacts on other classes of manufacturing systems.

Acknowledgment

The authors would like to acknowledge support from the NSF Award CMMI-1727894 and the NSF Engineering Research Center for Hybrid Autonomous Manufacturing Moving from Evolution to Revolution (ERC-HAMMER) under Award Number EEC-2133630. The authors would like to acknowledge Kevin Wolf from the Ohio State University for his assistance with system design and fabrication and Brian Iezzi and Zahra Afkhami from the University of Michigan for their discussion about the experimental testing.

Conflict of Interest

There are no conflicts of interest.

Data Availability Statement

The datasets generated and supporting the findings of this article are obtainable from the corresponding author upon reasonable request.

Appendix

A.1 Multi Excitation Filtering. The tone burst signal, Eq. (3), has the favorable property that the excitation is brief, on the order of microseconds, and thus permits temporal separation between the primary transmission and internal reflections in the PnC; however, the tone burst bandwidth is $1.441(f_0/M)$, which is on the order of 0.25-0.50 MHz for the fundamental frequencies used here [31]. To ensure a strong signal-to-noise ratio across a broad band of frequencies of interest, we excite the reference sample or

PnC with a sequence of temporally separated tone burst signals with different fundamental frequencies, $f_0 = 0.250$, 0.354, 0.500, ..., 5.66 MHz. Both time-domain transmission functions, $v_r(t)$ and $v_{\rm PnC}(t)$, are transformed to the frequency domain using the discrete Fourier transform (DFT) to give $V_r(f) = {\rm DFT}(v_r(t))$ and $V_{\rm PnC}(f) = {\rm DFT}(v_{\rm PnC}(t))$. Each frequency domain function is then multiplied by a frequency localizing basis functions (Fig. 11) to locally weight the response in the frequency band excited by its respective tone burst signal [31], Eq. (A1), and then summed together to form a composite frequency domain response across a broad band of frequencies, Eq. (A2).

$$F_k(s) := s^{q(k-1)} p_k^q \prod_{i=1}^k \frac{1}{(s+p_i)^q}; \quad k = 1, \dots, \tilde{n}$$
 (A1)

$$V_r(f) = \sum_{k=1}^{\tilde{n}+1} V_{r,k}(f) \left| F_k\left(j\frac{f}{2\pi}\right) \right| e^{j \angle F_k\left(j(f/2\pi)\right)}$$

$$V_{\text{PnC}}(f) = \sum_{k=1}^{\tilde{n}+1} V_{\text{PnC},k}(f) \left| F_k \left(j \frac{f}{2\pi} \right) \right| e^{j \angle F_k \left(j(f/2\pi) \right)} \quad (A2)$$

where $j = \sqrt{-1}$, $q \in \mathbb{N}_+$ is the order of basis function, and $0 < p_1 < \cdots < p_{\tilde{n}} < \infty$. The transmission spectra are then calculated using the standard equation

$$\left|T(f)\right| = \frac{|V_{\text{PnC}}(f)|}{|V_{r}(f)|} \tag{A3}$$

Here, we use q = 1 and $\mathbf{p} = (3/5)f_0$.

A.2 Transmission Spectra Metric Identification. Transmission spectra metrics f_c and w are identified from the transmission spectra |T(f)|. Each transmission spectra is fit to the bimodal Gaussian function

$$k(f) = a_1 e^{-(f - f_{c_1})^2 / 2\sigma_1^2} + a_2 e^{-(f - f_{c_2})^2 / 2\sigma_2^2}$$
(A4)

using the fit function in matlab. $f_{c(\cdot)}$ and $\sigma_{(\cdot)}$ are selected from the dominant peak, as determined by the maximum of a_1 and a_2 , as the metrics for f_c and w, respectively. w is calculated from $\sigma_{(\cdot)}$ using the -3 dB bandwidth convention:

$$w = 2\sigma_{(\cdot)}\sqrt{-2\ln(10^{-3/20})}$$
 (A5)

A.3 Consistency Between Training and Validation Data.

Figure 12 provides a comparison between training data and validation data for each loss function and metric pair. As validation artifacts are manufactured at design parameters that are not in the set of design parameters used in training, the validation data are compared to the four nearest neighbors in the set of design parameter used in training. Qualitatively, the validation data are largely within the span of the training data and are thus consistent.

References

- Montgomery, D. C., 2013, Design and Analysis of Experiments, 8th ed., John Wiley & Sons, Inc., Hoboken, NJ.
- [2] Xu, X., Vallabh, C. K. P., Cleland, Z. J., and Cetinkaya, C., 2017, "Phononic Crystal Artifacts for Real-Time In Situ Quality Monitoring in Additive Manufacturing," J. Manuf. Sci. Eng., 139(9), p. 091001.
- [3] Warmuth, F., Wormser, M., and Körner, C., 2017, "Single Phase 3D Phononic Band Gap Material," Sci. Rep., 7(1), pp. 1–7.

- [4] McGee, O., Jiang, H., Qian, F., Jia, Z., Wang, L., Meng, H., Chronopoulos, D., Chen, Y., and Zuo, L., 2019, "3D Printed Architected Hollow Sphere Foams With Low-Frequency Phononic Band Gaps," Addit. Manuf., 30, p. 100842.
- [5] Kruisová, A., Ševčík, M., Seiner, H., Sedlák, P., Román-Manso, B., Miranzo, P., Belmonte, M., and Landa, M., 2018, "Ultrasonic Bandgaps in 3D-Printed Periodic Ceramic Microlattices," Ultrasonics, 82, pp. 91–100.
- [6] Chen, Y., 2015, "Nanofabrication by Electron Beam Lithography and Its Applications: A Review," Microelectron. Eng., 135, pp. 57–72.
- [7] Zhan, A., Gibson, R., Whitehead, J., Smith, E., Hendrickson, J. R., and Majumdar, A., 2019, "Controlling Three-Dimensional Optical Fields Via Inverse Mie Scattering," Sci. Adv., 5(10), p. eaax4769.
- [8] Kolken, H. M., and Zadpoor, A., 2017, "Auxetic Mechanical Metamaterials," RSC Adv., 7(9), pp. 5111–5129.
- [9] Anderson, I. A., Gisby, T. A., McKay, T. G., O'Brien, B. M., and Calius, E. P., 2012, "Multi-functional Dielectric Elastomer Artificial Muscles for Soft and Smart Machines," J. Appl. Phys., 112(4), p. 041101.
- [10] King, R. D., Rowland, J., Oliver, S. G., Young, M., Aubrey, W., Byrne, E., Liakata, M., Markham, M., Pir, P., and Soldatova, L. N., 2009, "The Automation of Science," Science, 324(5923), pp. 85–89.
- [11] Williams, K., Bilsland, E., Sparkes, A., Aubrey, W., Young, M., Soldatova, L. N., De Grave, K., Ramon, J., De Clare, M., and Sirawaraporn, W., 2015, "Cheaper Faster Drug Development Validated by the Repositioning of Drugs Against Neglected Tropical Diseases," J. R. Soc. Interface, 12(104), p. 20141289.
- [12] Nikolaev, P., Hooper, D., Webber, F., Rao, R., Decker, K., Krein, M., Poleski, J., Barto, R., and Maruyama, B., 2016, "Autonomy in Materials Research: A Case Study in Carbon Nanotube Growth," npj Comput. Mater., 2(1), pp. 1–6.
- [13] Burger, B., Maffettone, P. M., Gusev, V. V., Aitchison, C. M., Bai, Y., Wang, X., Li, X., Alston, B. M., Li, B., and Clowes, R., 2020, "A Mobile Robotic Chemist," Nature, 583(7815), pp. 237–241.
- [14] Arinez, J. F., Chang, Q., Gao, R. X., Xu, C., and Zhang, J., 2020, "Artificial Intelligence in Advanced Manufacturing: Current Status and Future Outlook," J. Manuf. Sci. Eng., 142(11), p. 110804.
- [15] Gerling, A., 2022, "Towards an Implementation of an AutoML Tool for Manufacturing: Requirements, Improvements and First Results," Ph.D. thesis, Université de Haute Alsace, Mulhouse, France.
- [16] Krauß, J., Pacheco, B. M., Zang, H. M., and Schmitt, R. H., 2020, "Automated Machine Learning for Predictive Quality in Production," Procedia CIRP, 93, pp. 443–448.
- [17] Murphy, K. P., 2012, Machine Learning: A Probabilistic Perspective, MIT Press, Cambridge, MA.
- [18] Piovarči, M., Foshey, M., Xu, J., Erps, T., Babaei, V., Didyk, P., Rusinkiewicz, S., Matusik, W., and Bickel, B., 2022, "Closed-Loop Control of Direct Ink Writing Via Reinforcement Learning," ACM Trans. Graph., 41(4), p. 112.
- [19] Deneault, J. R., Chang, J., Myung, J., Hooper, D., Armstrong, A., Pitt, M., and Maruyama, B., 2021, "Toward Autonomous Additive Manufacturing: Bayesian Optimization on a 3D Printer," MRS Bulletin, 46, pp. 566–575.
- [20] Boyd, S. P., and Vandenberghe, L., 2004, Convex Optimization, Cambridge University Press, Cambridge.
- [21] Lim, I., Hoelzle, D. J., and Barton, K. L., 2017, "A Multi-Objective Iterative Learning Control Approach for Additive Manufacturing Applications," Control Eng. Pract., 64, pp. 74–87.
- [22] Deymier, P. A., 2013, Acoustic Metamaterials and Phononic Crystals, Vol. 173, Springer Science & Business Media, Berlin, Germany.
- [23] Alam, M. F., Shtein, M., Barton, K., and Hoelzle, D. J., 2020, "Autonomous Manufacturing Using Machine Learning: A Computational Case Study With a Limited Manufacturing Budget," Proceedings of the ASME Manufacturing Science and Engineering Conference, Cincinnati, OH, p. V002T07A009.
- [24] Linkwitz, S., 1980, "Shaped Tone-Burst Testing," J. Audio Eng. Soc., 28(4), pp. 250–258.
- [25] Xia, B., Chen, N., Xie, L., Qin, Y., and Yu, D., 2016, "Temperature-Controlled Tunable Acoustic Metamaterial With Active Band Gap and Negative Bulk Modulus," Appl. Acoust., 112, pp. 1–9.
- [26] Ambardar, A., 1995, Analog and Digital Signal Processing (A Volume in the PWS BookWare Companion Series), 2nd ed., Cengage Learning, Boston, MA.
- [27] Hastie, T., Tibshirani, R., and Friedman, J., 2009, The Elements of Statistical Learning: Data Mining, Inference, and Prediction, Springer Science & Business Media, New York.
- [28] Storn, R., and Price, K., 1997, "Differential Evolution—A Simple and Efficient Heuristic for Global Optimization Over Continuous Spaces," J. Global Optim., 11(4), pp. 341–359.
- [29] Alam, M. F., Shtein, M., Barton, K., and Hoelzle, D. J., 2021, "A Physics Guided Reinforcement Learning Framework for an Autonomous Manufacturing System With Expensive Data," Proceedings of the IEEE American Control Conference, New Orleans, LA, May 25–28, pp 484–490.
- [30] Alam, M. F., Shtein, M., Barton, K., and Hoelzle, D., 2023, "Reinforcement Learning Enabled Autonomous Manufacturing Using Transfer Learning and Probabilistic Reward Modeling," IEEE Control Syst. Lett., 7, pp. 508–513.
- [31] Welsh, J. S., and Rojas, C. R., 2007, "Frequency Localising Basis Functions for Wide-Band System Identification: A Condition Number Bound for Output Error Systems," 2007 European Control Conference (ECC), Kos, Greece, July 2–5, IEEE, pp. 4618–4624.